

Physics-informed PointNet: On how many irregular geometries can it solve an inverse problem simultaneously? Application to linear elasticity

Ali Kashefi ^{a*}, Leonidas J. Guibas ^b, Tapan Mukerji ^c

^aDepartment of Civil and Environmental Engineering, Stanford University, Stanford, CA, 94305 USA

^bDepartment of Computer Science, Stanford University, Stanford, CA, 94305 USA

^cDepartment of Energy Science and Engineering, Stanford University, Stanford, CA, 94305 USA

*Corresponding author: Ali Kashefi, kashefi@stanford.edu

Abstract

Regular physics-informed neural networks (PINNs) predict the solution of partial differential equations using sparse labeled data but only over a single domain. On the other hand, fully supervised learning models are first trained usually over a few thousand domains with known solutions (i.e., labeled data) and then predict the solution over a few hundred unseen domains. Physics-informed PointNet (PIPNet) is primarily designed to fill this gap between PINNs (as weakly supervised learning models) and fully supervised learning models. In this article, we demonstrate for the first time that PIPNet predicts the solution of desired partial differential equations over a few hundred domains simultaneously, while it only uses sparse labeled data. This framework benefits fast geometric designs in the industry when only sparse labeled data are available. Particularly, we show that PIPNet predicts the solution of a plane stress problem over more than 500 domains with different geometries, simultaneously. Moreover, we pioneer implementing the concept of remarkable batch size (i.e., the number of geometries fed into PIPNet at each sub-epoch) into PIPNet. We systematically try batch sizes of 7, 14, 19, 38, 76, and 133. Additionally, we systematically investigate for the first time the effect of the PIPNet size, symmetric function in the PIPNet architecture, and static and dynamic weights for the component of the sparse labeled data in the PIPNet loss function.

Keywords: Physics-informed PointNet; Irregular geometries; Linear elasticity; Inverse problems

Highlights

1. Similar to supervised deep learning, for the first time we test big data (i.e., number of geometry) and relatively large batch sizes (i.e., number of geometries per epoch) for the framework of physics-informed neural networks.
2. We specifically use PIPNet as an advanced version of physics-informed neural networks.
3. Using PIPNet, an inverse problem of linear elasticity is solved over 532 irregular geometries simultaneously.
4. Batch sizes (i.e., number of geometries per epoch) of 7, 14, 19, 28, 38, 76, and 133 are tested.
5. The effect of the PIPNet size and symmetric function in the PIPNet architecture are explored for the first time.

1 Introduction and motivation

Physics-informed Neural Networks (PINNs), introduced by Raissi, et al. [47] in 2019, are recognized as a promising tool for solving inverse problems in a variety of scientific and industrial fields such as solid mechanics [16, 48, 22, 53, 56, 62, 13, 8, 60, 3, 17, 5, 38, 50, 20, 46, 12], incompressible and compressible flows [23, 26, 35, 19, 18, 47, 40, 45, 39, 6], chemistry [59, 21], heat transfer [26, 57, 7], flow in porous media [28, 2, 65], etc. The main idea of PINNs for solving inverse problems can be briefly explained as follows. Given sparse observations of a field of interest as well as the partial differential equations (PDEs) governing the physics of the field, train “a neural network” such that its predictions (outputs) minimize the residuals of the PDEs as well as the distance between the predictions and sparse observations at sensor locations, in a certain norm (such as L^2 norm or other norms).

Other partial information such as boundary or initial conditions may be included in this minimization problem. Our focus, here, is on the term “a neural network”. We believe that the choice of the neural network significantly affects the ability and capacity of a PINN configuration. A common choice is a fully connected neural network (e.g., see Fig. 1 in Ref. [48], Fig. 3 in Ref. [16], Fig. 2 in Ref. [63], Fig. 1 in Ref. [35], Fig. 3 in Ref. [66], Fig 1 in Ref. [64], Fig. 1 in Ref. [36], Fig. 4 in Ref. [33], Fig. 1 in Ref. [11], etc.). An immediate consequence of this choice is that a PINN with a fully connected neural network is only able to predict the solution of an inverse problem on a single geometry. Hence, for any computational domain with a new geometry, one needs to train a PINN from scratch. This scenario necessitates high computational expenses, specifically when the goal is the investigation of a wide range of geometric parameters for optimizing an industrial design. This issue has been first addressed by Gao, et al. [14] in 2021 and later by Kashefi and Mukerji [26] in 2022.

To resolve this issue, Gao, et al. [14] first proposed the PhyGeoNet [14] framework and later Kashefi and Mukerji [26] introduced the PIPN [26] framework. PIPN [26] also successfully overcame the shortcomings of PhyGeoNet [14]. We later compare PIPN [26] versus PhyGeoNet [14], but for now, let us focus on the main theme of our article. What was one of the main motivations for introducing PIPN? To answer this question, let us discuss PINNs from another perspective. PINNs can be categorized as weakly supervised learning frameworks in the sense that the associated neural networks predict the solution on a computational domain using some sparse labeled data, which are available on that specific domain. On the other hand, neural networks used in supervised learning methods for computational mechanics are first trained on a large number of computational domains with different geometries, where the solutions are known, and then they predict the solution on new computational domains with new geometries. Supervised learning methods are commonly trained on a few hundred to a few thousand geometries (e.g., 2595 in Ref. [29], 1505 in Ref. [55], 880 in Ref. [51], 1600 in Ref. [9], etc.). One of the goals of introducing PIPN was to fill the gap between the weakly-supervised learning and supervised learning models in terms of the number of geometries for which we can predict the solution simultaneously (see Fig. 1). Now, the question is given the current capacity of available commercial graphics processing units (GPUs) to the public, how many computational domains (with different geometries) is PIPN able to predict the solution of an inverse problem on, simultaneously?

The answer to this question depends on different parameters. But definitely one of them is the level of complexity of a problem, which has a direct relevancy to its governing PDEs. When Kashefi and Mukerji [26] introduced PIPN, they [26] showed its applications for incompressible flows and natural convection, where the governing PDEs are nonlinear (see Eqs. 1–3 of Ref. [26]). Due to the nonlinearity of the problem, they had to select high resolutions (number of inquiry points) per computational domain. Specifically for the natural convection problem (see Sect. 4.2 of Ref. [26]), they run PIPN on 108 geometries, while each geometry had a resolution of 5000 inquiry points. They [26] further showed the effect of resolution on the accuracy of the PIPN prediction (see Fig. 18 of Ref. [26]). Because of the current limitations on GPU memories, they were not able to explore a “big” data set comparable to those used in supervised learning. One way to reduce the complexity level is to select a set of linear PDEs to examine the PIPN capacity. A reasonable choice is the equations of two-dimensional linear elasticity problems, which have a wide range of applications in the industry. Hence, to examine the capacity of PIPN in terms of simultaneous handling of the maximum possible number of geometries, we focus on the two-dimensional linear elasticity problems. Additionally, it is worth noting that this is the first time that PIPN is used for solving an inverse problem of linear elasticity.

An important hyperparameter that needs to be tuned for training neural networks in supervised learning of computational mechanics is “batch size”. The concept of “batch size” is defined under the category of mini-batch gradient descent [15], where the training data set is split into smaller data sets as mini-batches. The size of each mini-batch is then called “batch size”. The batch size plays a critical role in the training convergence as well as the ability of a trained neural network to generalize predictions [24, 30, 4, 37]. In supervised deep learning of quantities of interest as a function of geometric features of domains, the term batch size refers to the number of domains, with different geometries, that are fed to a neural network at each epoch. In regular PINNs, however, the term batch size refers to the number of inquiry points belonging to a sub-domain of a single domain that is fed to a neural network at each epoch. In PIPN, Kashefi and Mukerji [26] used the term batch size to address the number of domains at each epoch, similar to the scenario for supervised learning. Nevertheless, the maximum batch size was 13 as reported in their research article [26], again due to the GPU memory limitations and nonlinearity of their considered PDEs. In this article, we investigate for the first time a wide range of batch sizes and their influences on the training convergence and generalizability of PIPN with its applications to a linear elasticity problem.

Furthermore, we study for the first time another important hyperparameter, which is the network size of PIPN. In the framework of regular PINNs, where fully connected layers are used, the network size is tuned by changing the number of layers and a number of neurons in each layer. Contrarily to regular PINNs, PIPN has a more complicated architecture, and its network size can practically vary in different ways. In this work, we define a global scalar variable to control the network size of PIPN. Afterward, we study the performance of the PIPN framework as a function of this global variable.

Moreover, we investigate for the first time the effect of static and dynamic weights of the different components of the PIPN loss function on the PIPN performance in terms of both convergence rate and prediction accuracy. In addition, we explore for the first time the influence of symmetric functions, embedded in the PIPN architecture,

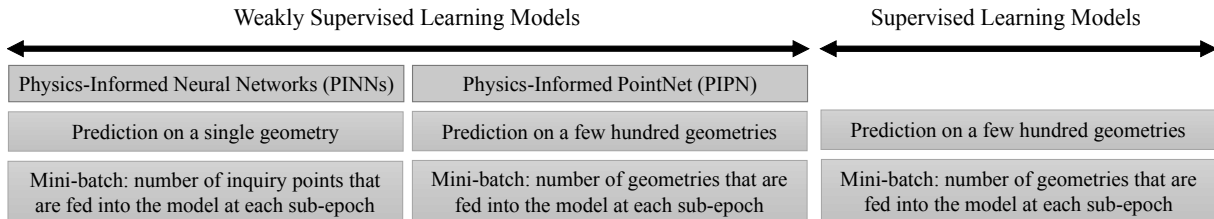


Figure 1: A conceptual comparison between regular physics-informed neural networks (PINNs), physics-informed PointNet (PIPNet), and fully supervised deep learning algorithms for computational mechanics in terms of the number of geometries and the batch size definition

on the accuracy of the PIPNet outputs.

For the sake of completeness and also convincing the potential audiences why we go with PIPNet [26] rather than PhyGeoNet [14] in this article, we compare PIPNet [26] with PhyGeoNet [14]. In PhyGeoNet [14], a convolutional neural network (CNN) is used as the “neural network” in a PINN, instead of a fully connected neural network. CNNs are able to extract geometric features of input computational domains and represent those features in a hidden space. Hence, all the parameters of CNNs (e.g., weights and bias) become a function of the geometric features. As a result, PhyGeoNet [14] is able to solve an inverse problem on multiple sets of computational domains. Notwithstanding these successes, PhyGeoNet [14] and its later version [49] come with several shortcomings. These shortcomings have been addressed in detail in Sect. 1 of Ref. [26]. Here, we summarize them. First, PhyGeoNet [14] uses a finite difference discretization method for computing the loss function of desired PDEs rather than using the automatic differentiation technology [1]. In this way, PhyGeoNet [14] is limited to the accuracy order of the chosen finite difference scheme and faces challenges for treating near boundaries of computational domains in the case of using high-order finite difference methods. Second, PhyGeoNet [14] is not able to handle irregular “non-parameterizable” geometries. Third, even on irregular parameterizable geometries, PhyGeoNet [14] is strictly limited to handling domains with up to only five C_0 continuous boundaries.

To obviate the limitations of PhyGeoNet [14], Kashefi and Mukerji [26] introduced physics-informed PointNet (PIPNet). In PIPNet, PointNet [43] carries out the role of the “neural network” in PINNs. Similar to CNNs, PointNet [43] is able to also encode the geometric features of input computational domains; however, using a different mathematical methodology. Introduced in 2017, PointNet [43] emerged as a prominent deep learning model for addressing 3D computer vision problems such as shape classification and segmentation. PointNet [43] set the stage for subsequent research, such as object detection in both outdoor [42] and indoor [41] environments, and the prediction of scene flow from sequential point cloud data [34]. The classification branch of PointNet [43] was also used for identifying structure in molecular simulations [10] and atomistic simulations [52] as well as predicting porous medium permeability [25]. Although advanced versions of PointNet have surfaced, with adaptations like hierarchical PointNet [44] and innovative approaches utilizing graph [58] or continuous convolutions [54] on point clouds, the original PointNet [43] continues to stand out for its conceptual and computational simplicity. Details of the PointNet architecture can be found in Refs. [43, 29, 26, 25]. We also briefly review the PointNet structure in Sect. 2.2 of this research paper. The advantages of PIPNet compared to PhyGeoNet have been explained in detail by Kashefi and Mukerji [26]. We list them here for a quick review. First and most important, PIPNet [26] can handle non-parametrizable irregular geometries without any restriction. Second, PIPNet [26] uses automatic differentiation technology [1] and thus the spatial derivative of output components with respect to the corresponding input component can be conveniently programmed and computed over entire irregular geometries in a data set (with no need for a finite difference/element discretization). Third, in the PIPNet framework, interior and boundary points of irregular geometries are explicitly identified, and it allows twofold benefits: first, a smooth representation of boundaries (e.g., an airfoil surface), and second, explicit identification of their corresponding components in the loss function (with no need for implicit labeling of boundary points versus interior points and an artificial mixing up near boundaries, especially with sharp corners).

The rest of this research paper is structured as follows. We mathematically formulate the linear elasticity problem in Sect. 2.1. An illustration of PIPNet from computer science and applied mathematics perspectives are given in Sect. 2.2. Details about generating data for validation of the PIPNet framework are described in Sect. 2.3. We elaborate on the computational setup for training PIPNet in Sect. 2.4. A general analysis of the PIPNet performance as well as the effect of batch size and neural network size is discussed in Sect. 3. Concluding remarks are listed in Sect. 4.

2 Problem statement and methodologies

2.1 Problem formulations

In this article, we focus on elastic materials with the constitutive model of Hooke’s law, relating the Cauchy stress tensor to the infinitesimal strain tensor and we restrict our studies to isotropic materials under plane stress assumptions. Specifically, we consider a two-dimensional domain V having a cavity space characterized by various shapes. The domain V is placed under a thermal conductivity loading. The static linear elasticity equations governing the displacement fields in the domain V are given by

$$-\frac{\partial}{\partial x} \left(\frac{E}{1-\nu^2} \frac{\partial u}{\partial x} + \frac{E\nu}{1-\nu^2} \frac{\partial v}{\partial y} \right) - \frac{\partial}{\partial y} \left(\frac{E}{2(1+\nu)} \left(\frac{\partial u}{\partial y} + \frac{\partial v}{\partial x} \right) \right) = -\frac{E\alpha}{1-\nu^2} \frac{\partial T}{\partial x}, \quad (1)$$

$$-\frac{\partial}{\partial y} \left(\frac{E\nu}{1-\nu^2} \frac{\partial u}{\partial x} + \frac{E}{1-\nu^2} \frac{\partial v}{\partial y} \right) - \frac{\partial}{\partial x} \left(\frac{E}{2(1+\nu)} \left(\frac{\partial u}{\partial y} + \frac{\partial v}{\partial x} \right) \right) = -\frac{E\alpha}{1-\nu^2} \frac{\partial T}{\partial y}, \quad (2)$$

where T indicates the temperature variable. Displacements in the x and y directions are shown by u and v , respectively. α denotes the thermal expansion coefficient. E is the elastic Young’s modulus and ν is the Poisson ratio. We assume that the material of the domain V remains in the elastic regime under thermal loading.

Mathematically, our goal is to solve an inverse problem using PIPN on a set of irregular domains $\Phi = \{V_i\}_{i=1}^m$, formulated as follows: given the temperature field of the domains $\Phi = \{V_i\}_{i=1}^m$ and a set of sparse observations of the displacement fields of the domains of the set $\Phi = \{V_i\}_{i=1}^m$, find the full displacement solutions for all the domains of the set $\Phi = \{V_i\}_{i=1}^m$. We explicitly illustrate geometric variations of the set $\Phi = \{V_i\}_{i=1}^m$ in Sect. 2.3.

2.2 Physics-informed PointNet (PIPNet)

As we discussed in Sect. 1, the idea of PIPN was first proposed by Kashefi and Mukerji [26] in 2022. Here, we briefly review the PIPN methodology and adjust it for the governing equations of our interest (Eqs. 1–2). PIPN is built based on the combination of two critical pieces: PointNet [43] and a physics-based loss function. In simple words, the PIPN mechanism can be explained in two steps. In the first step, PointNet [43] makes the predicted outputs as a function of geometric features of each $V_i \in \Phi$. As the second step, the PIPN loss function is computed by taking these outputs and manipulating them using automatic differentiation [1] to build up the equations describing the physics of the problem. Hence, the PIPN loss function is not only aware of the physics but also aware of the geometries of each $V_i \in \Phi$. In this way, by training PIPN, the predicted solutions for the displacement fields on a domain V_i become a function of the geometric characteristic of V_i . In this sense, PIPN is able to predict the solutions of the governing PDEs (Eqs. 1–2) on multiple computational domains with various geometries, simultaneously.

2.2.1 Architecture

The PIPN architecture is exhibited in Fig. 2. In PIPN, each V_i is represented by a point-cloud \mathcal{X}_i with N points. \mathcal{X}_i is defined as $\mathcal{X}_i = \{\mathbf{x}_j \in \mathbb{R}^d\}_{j=1}^N$, where d is the spatial dimension and we set $d = 2$ in this research study. Thus, each \mathbf{x}_j has two components x_j and y_j as the spatial coordinates. PIPN maps \mathcal{X}_i to \mathcal{Y}_i via a function f , where \mathcal{Y}_i is the prediction of the PDE (Eqs. 1–2) solutions. \mathcal{Y}_i is defined as $\mathcal{Y}_i = \{\mathbf{y}_j \in \mathbb{R}^{n_{\text{PDE}}}\}_{j=1}^N$, where n_{PDE} indicates the number of fields in the solution. Here, we set $n_{\text{PDE}} = 2$ as the displacement fields (u and v) are the unknowns. Hence, each \mathbf{y}_j has two components, u_j and v_j as the network outputs. Mathematically, it can be written as

$$(u_j, v_j) = f((x_j, y_j), g(\mathcal{X}_i)); \forall (x_j, y_j) \in \mathcal{X}_i \text{ and } \forall (u_j, v_j) \in \mathcal{Y}_i \text{ with } 1 \leq i \leq m \text{ and } 1 \leq j \leq N, \quad (3)$$

where f is the mapping function approximated by the PointNet [43] neural network and g is a symmetric function representing the geometric feature of a point cloud \mathcal{X}_i and can be approximated as

$$g(\mathcal{X}_i) = s(h(x_1, y_1), \dots, h(x_N, y_N)); \forall (x_j, y_j) \in \mathcal{X}_i \text{ with } 1 \leq i \leq m \text{ and } 1 \leq j \leq N, \quad (4)$$

where s is a symmetric function and h is a function representing the two shared Multilayer Perceptrons (MLPs) [32, 43, 44] in the first branch of PointNet [43] (see Fig. 2). In simple words, $g(\mathcal{X}_i)$ can be thought as the global feature in the PIPN architecture shown in Fig. 2. We further explain the role of shared MLPs and the symmetric function in the following. We define n_s as a global scaling variable controlling the size of the PIPN. In the following, we denote batch size by B , and reemphasize that “batch size” in this study is the number of domains fed into PIPN at each epoch.

In practice, the input of PIPN is a three-dimensional tensor (i.e., numeric array) of size $B \times N \times 2$. Afterward, there are two sequential shared MLPs with sizes of $(n_s \times 64, n_s \times 64)$ and $(n_s \times 64, n_s \times 128, n_s \times 1024)$, as displayed in Fig. 2. In the next step, the symmetric operator (s) forms the global feature with a size of $n_s \times 1024$. As exhibited in Fig. 2, the global feature is concatenated to the intermediate feature tensor of size $B \times N \times (n_s \times 64)$, resulting in a tensor of size $B \times N \times (n_s \times 1088)$. Next, two other sequential shared MLPs, respectively, with sizes of $(n_s \times 512, n_s \times 256, n_s \times 128)$ and $(n_s \times 128, n_{\text{PDE}})$ operate in the PIPN architecture. The output of the

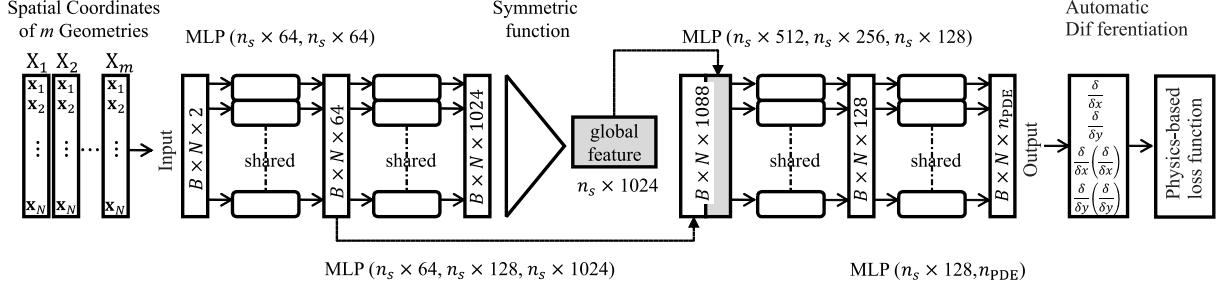


Figure 2: Architecture of physics-informed PointNet (PIPNet); B indicates the batch size and n_s is a global scaling parameter for controlling the network size. The spatial derivatives are computed using automatic differentiation to build up the residuals of the governing PDEs as the PIPNet loss function.

previous action is a tensor of size $B \times N \times n_{\text{PDE}}$, as shown in Fig. 2. Using automatic differentiation [1], the governing PDEs (Eqs. 1–2) are built and fed into the PIPNet loss function. Note that reasonable choices for n_s could be 0.125, 0.25, 0.5, 1.0, 2.0, and 4.0 such that a positive integer number represents the size of resulting shared MLPs.

2.2.1.1 Shared MLPs and symmetric functions

The PIPNet is invariant with respect to $N!$ permutations of the input vector (see Fig. 2). In other words, if we randomly permute the input vector (\mathcal{X}_i), the constructed geometry of the domain does not change and thus the solution (\mathcal{Y}_i) should not change. PIPNet becomes permutation invariant by means of two features: shared MLPs and symmetric functions.

The concept of shared MLPs should not be confused with regular fully connected layers or so-called “dense” layers in the TensorFlow [1] terminology. Here we explain the concept of shared MLPs with a simple example. Let us consider the first MLP layer in the first branch of PIPNet with a size of $(n_s \times 64, n_s \times 64)$ as shown in Fig. 2. Let us take $n_s = 1$ for a moment. More specifically, we focus on the first shared layer with a size of 64. The transpose of the input vector \mathcal{X}_i can be written as

$$\mathcal{X}_i^{tr} = \begin{bmatrix} x_1 & x_2 & \dots & x_N \\ y_1 & y_2 & \dots & y_N \end{bmatrix}. \quad (5)$$

After applying the first shared layer to \mathcal{X}_i , the output is a matrix of size $64 \times N$ and can be written as

$$\begin{bmatrix} \mathbf{a}_{64 \times 1}^{(1)} & \mathbf{a}_{64 \times 1}^{(2)} & \dots & \mathbf{a}_{64 \times 1}^{(N)} \end{bmatrix}, \quad (6)$$

where $\mathbf{a}_{64 \times 1}^{(1)}, \mathbf{a}_{64 \times 1}^{(2)}, \dots, \mathbf{a}_{64 \times 1}^{(N)}$ are vectors, which are computed as follows

$$\begin{aligned} \mathbf{a}_{64 \times 1}^{(1)} &= \sigma \left(\mathbf{W}_{64 \times 2} \begin{bmatrix} x_1 \\ y_1 \end{bmatrix} + \mathbf{b}_{64 \times 1} \right), \\ \mathbf{a}_{64 \times 1}^{(2)} &= \sigma \left(\mathbf{W}_{64 \times 2} \begin{bmatrix} x_2 \\ y_2 \end{bmatrix} + \mathbf{b}_{64 \times 1} \right), \\ &\vdots \\ \mathbf{a}_{64 \times 1}^{(N)} &= \sigma \left(\mathbf{W}_{64 \times 2} \begin{bmatrix} x_N \\ y_N \end{bmatrix} + \mathbf{b}_{64 \times 1} \right), \end{aligned} \quad (7)$$

where \mathbf{W} and \mathbf{b} are the shared weight matrix and bias vector, respectively. The nonlinear activation function is shown by σ , which acts elementwise. As can be realized from Eq. 7, the same (shared) \mathbf{W} and \mathbf{b} are applied to each spatial point of the domain with the corresponding vector of $[x_j \ y_j]^{tr}$, while $1 \leq j \leq N$. That is why we call it shared MLPs. A similar procedure is conducted at the rest of the layers. By this strategy, it is immediately concluded that each point is independently processed in the PIPNet framework and the only place that points meet each other is where the global feature needs to be identified (see Eq. 4).

Concerning the symmetric function, we consider the two formats: one being the “maximum” function such that

$$g(\mathcal{X}_i) = \max(h(x_1, y_1), \dots, h(x_N, y_N)); \forall (x_j, y_j) \in \mathcal{X}_i \text{ with } 1 \leq i \leq m \text{ and } 1 \leq j \leq N, \quad (8)$$

and the other being the “average” function such that

$$g(\mathcal{X}_i) = \text{average}(h(x_1, y_1), \dots, h(x_N, y_N)); \forall (x_j, y_j) \in \mathcal{X}_i \text{ with } 1 \leq i \leq m \text{ and } 1 \leq j \leq N. \quad (9)$$

We compare the PIPN performance using these two symmetric functions. One may refer to Ref. [26] for a further description of the details of PIPN; and to Ref. [43] for a further discussion on the computer science aspects of PointNet [43].

2.2.2 Loss function

For any pair of \mathcal{X}_i and \mathcal{Y}_i ($1 \leq i \leq m$), the residuals of the linear momentum in the x direction ($\mathcal{J}_i^{\text{momentum}_x}$), linear momentum in the y direction ($\mathcal{J}_i^{\text{momentum}_y}$), along with the residuals of the sparse observations of the displacement field ($\mathcal{J}_i^{\text{displacement}_{\text{sensor}}}$) are respectively defined as follows:

$$\mathcal{J}_i^{\text{momentum}_x} = \frac{1}{N} \sum_{k=1}^N \left(-\frac{\delta}{\delta x_k} \left(\frac{1}{1-\nu} \frac{\delta \tilde{u}_k}{\delta x_k} + \frac{\nu}{1-\nu} \frac{\delta \tilde{v}_k}{\delta y_k} \right) - \frac{\delta}{\delta y_k} \left(\frac{1}{2} \left(\frac{\delta \tilde{u}_k}{\delta y_k} + \frac{\delta \tilde{v}_k}{\delta x_k} \right) \right) + \frac{\alpha}{1-\nu} \frac{\partial T_k}{\partial x_k} \right)^2, \quad (10)$$

$$\mathcal{J}_i^{\text{momentum}_y} = \frac{1}{N} \sum_{k=1}^N \left(-\frac{\delta}{\delta y_k} \left(\frac{\nu}{1-\nu} \frac{\delta \tilde{u}_k}{\delta x_k} + \frac{1}{1-\nu} \frac{\delta \tilde{v}_k}{\delta y_k} \right) - \frac{\delta}{\delta x_k} \left(\frac{1}{2} \left(\frac{\delta \tilde{u}_k}{\delta y_k} + \frac{\delta \tilde{v}_k}{\delta x_k} \right) \right) + \frac{\alpha}{1-\nu} \frac{\partial T_k}{\partial y_k} \right)^2, \quad (11)$$

$$\mathcal{J}_i^{\text{displacement}_{\text{sensor}}} = \frac{1}{M} \sum_{k=1}^M \left(\left(\tilde{u}_k - u_k^{\text{sensor}} \right)^2 + \left(\tilde{v}_k - v_k^{\text{sensor}} \right)^2 \right), \quad (12)$$

where M is the number of sensors located at each point cloud for a sparse measurement of the displacement fields. The automatic differentiation operator is shown by δ . The x and y components of the displacement fields measured at the sensor locations are shown by u_k^{sensor} and v_k^{sensor} , respectively, while the network outputs are denoted by \tilde{u}_k and \tilde{v}_k . Note that because we assume that the temperature field is known to us, then the temperature gradient is also known. The hyperbolic activation function defined as

$$\sigma(\gamma) = \frac{e^{2\gamma} - 1}{e^{2\gamma} + 1}, \quad (13)$$

is implemented in all the layers of PIPN, similar to Refs. [26, 28]. Note that due to the presence of the second-order spatial derivative of the displacement fields in the governing PDEs (Eqs. 1–2), the second-order derivative of the activation function used in PIPN must be well-defined.

As can be realized from Eq. 3, because the displacement fields are a function of $g(\mathcal{X}_i)$, the spatial derivatives of the displacement also become a function of $g(\mathcal{X}_i)$ in PIPN. For example,

$$\frac{\delta u_j}{\delta x_j} = \frac{\delta f((x_j, y_j), g(\mathcal{X}_i))}{\delta x_j}; \forall (x_j, y_j) \in \mathcal{X}_i \text{ and } \forall u_j \in \mathcal{Y}_i \text{ with } 1 \leq i \leq m \text{ and } 1 \leq j \leq N. \quad (14)$$

Similar expressions can be written for $\frac{\delta u_j}{\delta y_j}$, $\frac{\delta v_j}{\delta x_j}$, $\frac{\delta}{\delta x_j} \left(\frac{\delta u_j}{\delta x_j} \right)$, etc. Hence, all the components presented in the loss function of PIPN contain the geometric information of the point clouds of the set $\Phi = \{V_i\}_{i=1}^m$, a specific feature that is not available in regular PINNs [47]. Eventually, the PIPN loss function is written as

$$\mathcal{J} = \frac{B}{m} \sum_{b=1}^{m/B} \left(\frac{1}{B} \sum_{i=1+(b-1)B}^{bB} \left(\omega_{\text{momentum}} (\mathcal{J}_i^{\text{momentum}_x} + \mathcal{J}_i^{\text{momentum}_y}) + \omega_{\text{sensor}} \mathcal{J}_i^{\text{displacement}_{\text{sensor}}} \right) \right), \quad (15)$$

where ω_{momentum} and ω_{sensor} are the corresponding weights of each residual, while their units are the inverse of the unit of their associated residuals such that the total loss function (\mathcal{J}) becomes unitless at the end. We elaborate on the choice of these weight factors in the following section.

2.2.2.1 Component weights in the PIPN loss function

Based on our machine learning experiments, the choice of ω_{momentum} and ω_{sensor} remarkably affect the convergence rate of the training procedure. Here, we propose a few simple, but practical functions for ω_{momentum} and ω_{sensor} , and discuss their effects in Sect. 3. The first trivial selection is setting an equal weight for both the momentum and sensor components of the loss function such that

$$\begin{cases} \omega_{\text{momentum}} = 1 \text{ m} \\ \omega_{\text{sensor}} = 1 \text{ m}^{-1}. \end{cases} \quad (16)$$

The next choice is setting a higher weight for the sensor component compared to the momentum one in the PIPN loss function (see Eq. 13) such that

$$\begin{cases} \omega_{\text{momentum}} = 1 \text{ m} \\ \omega_{\text{sensor}} = \omega_0 \text{ m}^{-1}, \text{ with } \omega_0 > 1. \end{cases} \quad (17)$$

Note that ω_0 remains constant during the training and can be thought of as a hyperparameter. Additionally, our machine learning experiments show that setting a higher weight for the momentum component compared to the

Table 1: Description of the generated geometries; R indicates the radius of the circumscribed circle of the inner thin cavity. Ω denotes variation (in degree) in the orientation of the inner thin cavity with respect to its geometric center.

The shape of the inner thin cavity	R	Ω	Side length of thin square plates	Number of selected data
Square	0.35 m	1, 3, ..., 87, 89	1.6 m, 1.8 m, 2 m	134
Regular pentagon	0.30 m	1, 3, ..., 69, 71	1.6 m, 1.8 m, 2 m	107
Regular hexagon	0.30 m	1, 3, ..., 57, 59	1.6 m, 1.8 m, 2 m	90
Regular heptagon	0.30 m	1, 3, ..., 49, 51	1.6 m, 1.8 m, 2 m	76
Regular octagon	0.30 m	1, 3, ..., 43, 45	1.6 m, 1.8 m, 2 m	66
Regular nonagon	0.30 m	1, 3, ..., 37, 39	1.6 m, 1.8 m, 2 m	59
Total				532

sensor one leads to a significant reduction in the convergence speed and thus we do not propose it here. Our third proposal is setting a higher weight for the sensor component, while this weight exponentially decreases during the training process such that

$$\begin{cases} \omega_{\text{momentum}} = 1 \text{ m} \\ \omega_{\text{sensor}} = \max\left(\omega_1 \times \exp\left(\frac{-\text{epoch}}{r_1}\right), 1.0\right) \text{ m}^{-1}, \text{ with } \omega_1 > 1 \text{ and } r_1 > 0, \end{cases} \quad (18)$$

where ‘‘epoch’’ refers to the training iteration. Again, ω_1 and r_1 are the hyperparameters. Our last suggestion is similar to our third one with the difference that the weight decreases logarithmically such that

$$\begin{cases} \omega_{\text{momentum}} = 1 \text{ m} \\ \omega_{\text{sensor}} = \max\left(\omega_2 \times \ln(-\text{epoch} + r_2), 1.0\right) \text{ m}^{-1}, \text{ with } \omega_2 > 1 \text{ and } r_2 > 0, \end{cases} \quad (19)$$

where ω_2 and r_2 are the hyperparameters. Note that in all our proposals, ω_{sensor} never becomes less than one. Again, the units of ω_{momentum} and ω_{sensor} are set such that \mathcal{J} becomes unitless.

At the end of this subsection, we address the fact that setting optimal weights in the loss functions of deep learning models is an active research area by itself (see e.g., Ref. [61]); however, this is the first time that we introduce this concept to the PIPN configuration.

2.3 Data generation

Computational domains of the set $\Phi = \{V_i\}_{i=1}^m$ are thin square plates with a cavity. The side length of the square plates takes three different values while the cavity takes shapes of a square, regular pentagon, regular hexagon, regular octagon, and regular nonagon. We further enlarge the number of domains by rotating the cavity with respect to the fixed thin square plates. Details of the geometric features of the set $\Phi = \{V_i\}_{i=1}^m$ are listed in Table 1. In total, 532 geometries (i.e., $m = 532$) are the input of PIPN. In this way, we establish the set $\Phi = \{V_i\}_{i=1}^{532}$. Three examples of geometries of this set are shown in Fig. 3. Concerning the sensor locations, we initially assume the domains have no cavities and distribute sensors evenly within them. Any sensors located within the cavity are then relocated to the nearest point inside the domain. In our machine learning investigations, we consider batch sizes (B) of 7, 14, 19, 28, 38, 76, and 133, which are all divisors of 532. We recall that the maximum batch size (B) implemented by Kashefi and Mukerji [26] was 13 and the maximum number of input data (m) considered by Kashefi and Mukerji [26] was 108. Another difference is that the side length of the outer boundaries takes three values of 1.6 m, 1.8 m, and 2.0 m in the current study; however, Kashefi and Mukerji [26] exclusively considered a fixed value of 2.0 m for the side length of outer boundaries when they studied natural convection in a square enclosure with a cylinder (see Fig. 12 and Table 7 of Ref. [26]). In this way, we experience more variations in geometric features of the input point clouds in this study and thus a more challenging task is defined for PIPN.

The MATLAB PDE toolbox is used for the two purposes of validation of the PIPN predictions and generations of the sparse labeled data at virtual sensor locations. The ground truth data is generated using the toolbox as follows. The domains of the set $\Phi = \{V_i\}_{i=1}^{532}$ are loaded by thermal conduction with Dirichlet boundary conditions such that the temperature on the outer and inner boundaries are respectively set to 1 and zero in International Unit System. Note that the thermal conductivity does not affect the solution of the Laplace equation governing the steady-state thermal conduction. Moreover, we impose zero displacement boundary conditions on the boundaries of the domains of the set $\Phi = \{V_i\}_{i=1}^{532}$.

2.4 Computational considerations

The Poisson ratio (ν) is set to 0.3 and the thermal expansion coefficient (α) is set to 1.0 in the International Unit System. Note that elastic Young’s modulus (E) does not appear in Eqs. (10–11) and thus is not a problem input.

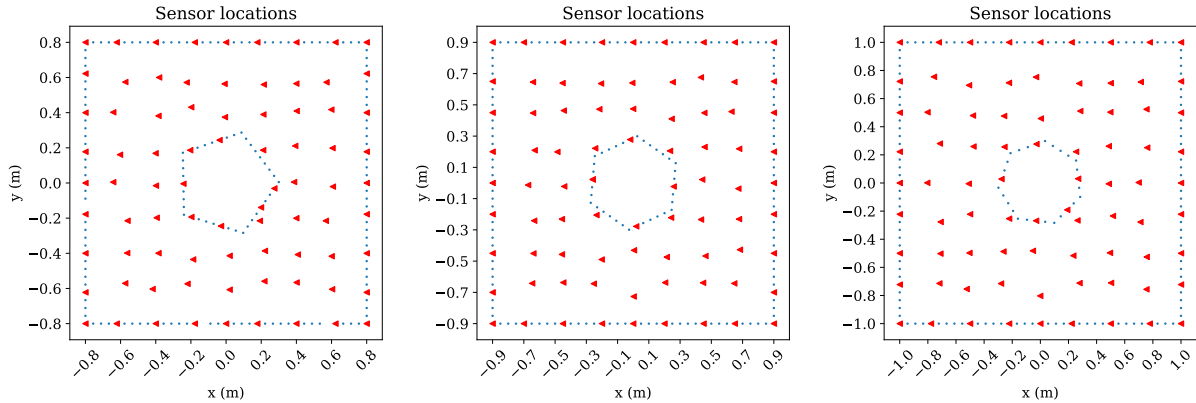


Figure 3: Sensor locations for three domains from the set $\Phi = \{V_i\}_{i=1}^{532}$; Red triangles show sensors measuring the displacement fields

Furthermore, we set $N = 2021$ and $M = 81$ in the point clouds. The sensors are approximately equally spaced and located in the domains of the set $\Phi = \{V_i\}_{i=1}^{532}$. The sensor locations for three different domains taken from the set $\Phi = \{V_i\}_{i=1}^{532}$ are exhibited, for instance, in Fig. 3. We use the Adam optimizer [31] with the hyperparameters of $\beta_1 = 0.9$, $\beta_2 = 0.999$, and $\hat{\epsilon} = 10^{-6}$. The mathematical explanation of β_1 , β_2 , and $\hat{\epsilon}$ are expressed in Ref. [31]. The constant learning rate of 0.0003 is set for the entire machine learning experiments. For a fair comparison, all the simulations are run with double precision on an NVIDIA A100 SXM4 graphic card with a memory clock rate of 1.41 GHz and 40 Gigabytes of RAM.

3 Results and discussion

3.1 General analysis

In Table 2, we tabulate the average, maximum, and minimum errors of the predicted displacement fields in the x and y directions for the domains of the set $\Phi = \{V_i\}_{i=1}^{532}$ with batch size of $B = 28$, the network size of $n_s = 1.0$, and the weight of $\omega_{\text{sensor}} = 50 \text{ m}^{-1}$ for the sensor component in the PIPN loss function (see Eq. 15). According to the data tabulated in Table 2, the average pointwise relative errors (L^2 norm) for all 532 geometries of the set Φ is less than 9%, indicating a successful accomplishment for the PIPN framework. Moreover, the maximum pointwise relative errors (L^2 norm) do not exceed 14%, demonstrating a reasonable accuracy for engineering applications.

A comparison between the ground truth (i.e., the finite element solutions) and the PIPN predictions is made in Figs. 4–6 for six different geometries taken from the set $\Phi = \{V_i\}_{i=1}^{532}$. As can be observed in Figs. 4–6, there is an excellent agreement between the ground truth and the displacement fields predicted by PIPN. For each geometry, the maximum local pointwise error happens on the boundaries of the inner cavity of thin plates. This outcome is expectable because, first, PIPN is not informed from boundary conditions (i.e., zero displacements), and second, most variations from one geometry to another one take place on the boundaries of the domains of the set $\Phi = \{V_i\}_{i=1}^{532}$. In fact, predicting boundary values is the most difficult task for PIPN during the training procedure. This fact can be realized by looking at Fig. 7. We exhibit the prediction of PIPN for the displacement fields for one geometry taken from the set $\Phi = \{V_i\}_{i=1}^{532}$ after 3, 500, and 1500 epochs. Based on what can be seen in Fig. 7, the PIPN prediction is inaccurate after 10 epochs. After 500 epochs, the displacement fields are accurately predicted by PIPN except on the boundaries of the domain. An improvement in the prediction of zero displacements on the boundaries of the domain is observed at the PIPN outcome after 1500 epochs. Hence, we conclude that the most time-consuming part for PIPN is to predict the right values on the domain boundaries.

The absolute pointwise error (L^2 norm) for geometries with the maximum and minimum relative pointwise errors of the displacement fields in the x and y directions are shown in Fig. 8. According to Fig. 8, the extremum errors occur for domains with different geometries of the set $\Phi = \{V_i\}_{i=1}^{532}$, revealing the fact that PIPN is not overfitted to one specific geometry. Moreover, we observe that the maximum pointwise errors happen for the domains with the side length of 1.6 m, which is the smallest side length available in the data set $\Phi = \{V_i\}_{i=1}^{532}$. On the other hand, the minimum pointwise errors occur for geometries with the side square length of 2.0 m, which is the largest available side length in the data set $\Phi = \{V_i\}_{i=1}^{532}$. Based on our deep learning experiments, the ideal range for the spatial coordinates of the input geometries is when they are expanded in $[-1, 1]$. Having stretched geometries out of $[-1, 1]$ or compressed geometries inside of $[-1, 1]$ results in an error increase. Therefore, the domains with a side length of 1.6 m end up having higher levels of errors compared to larger side lengths.

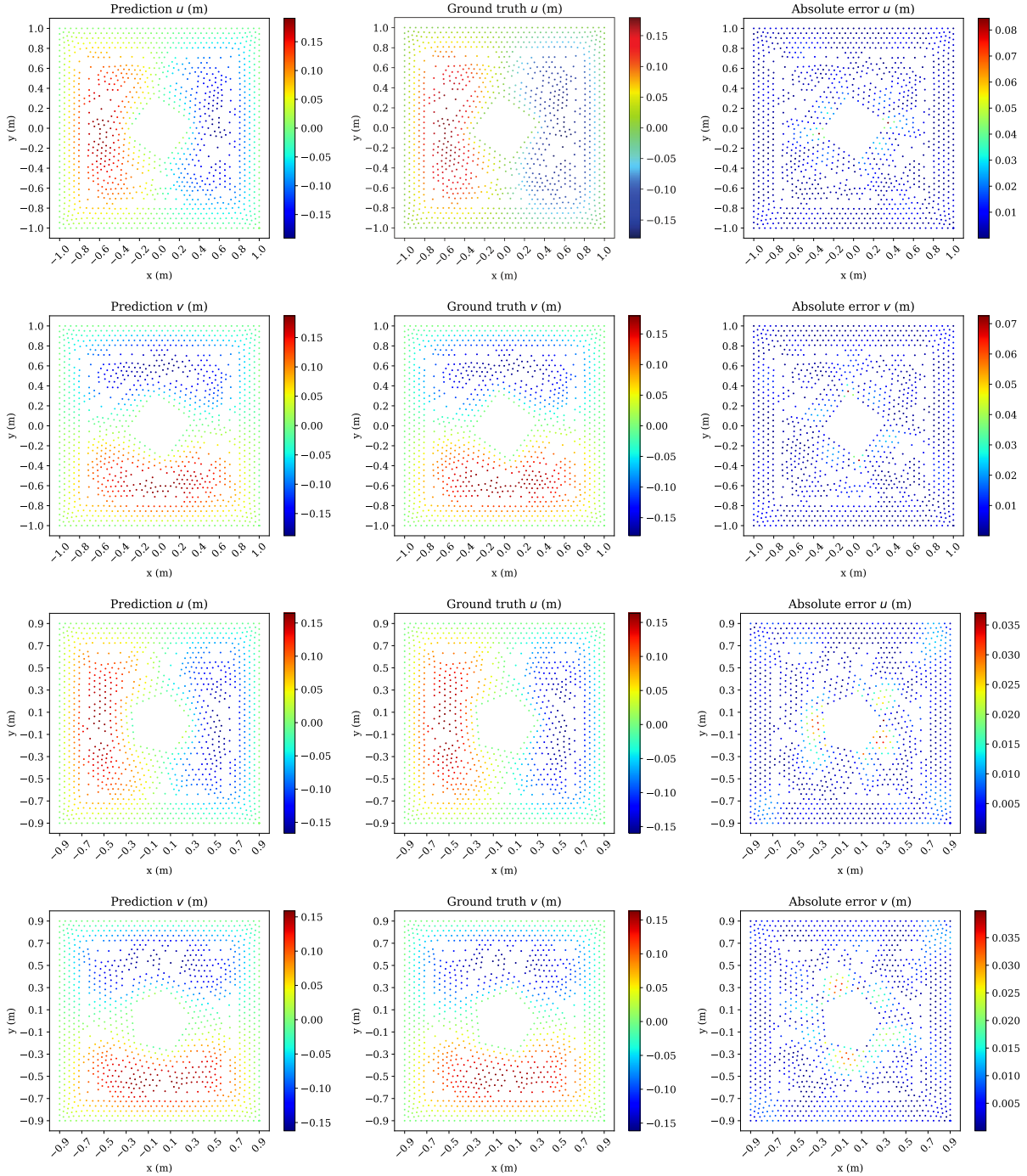


Figure 4: The first group of examples taken from the set $\Phi = \{V_i\}_{i=1}^{532}$, comparing the finite element solutions to the PIPN predictions for the displacement fields

Table 2: Error analysis of the displacement fields for the domains of the set $\Phi = \{V_i\}_{i=1}^{532}$ when $B = 28$, $n_s = 1$, $\omega_{\text{sensor}} = 50 \text{ m}^{-1}$, and $\omega_{\text{momentum}} = 1 \text{ m}$. $\|\dots\|$ indicates the L^2 norm.

	$\ \tilde{u} - u\ /\ u\ $	$\ \tilde{v} - v\ /\ v\ $
Average	8.11108E-2	8.60237E-2
Minimum	5.74907E-2	6.32261E-2
Maximum	1.19782E-1	1.31120E-1

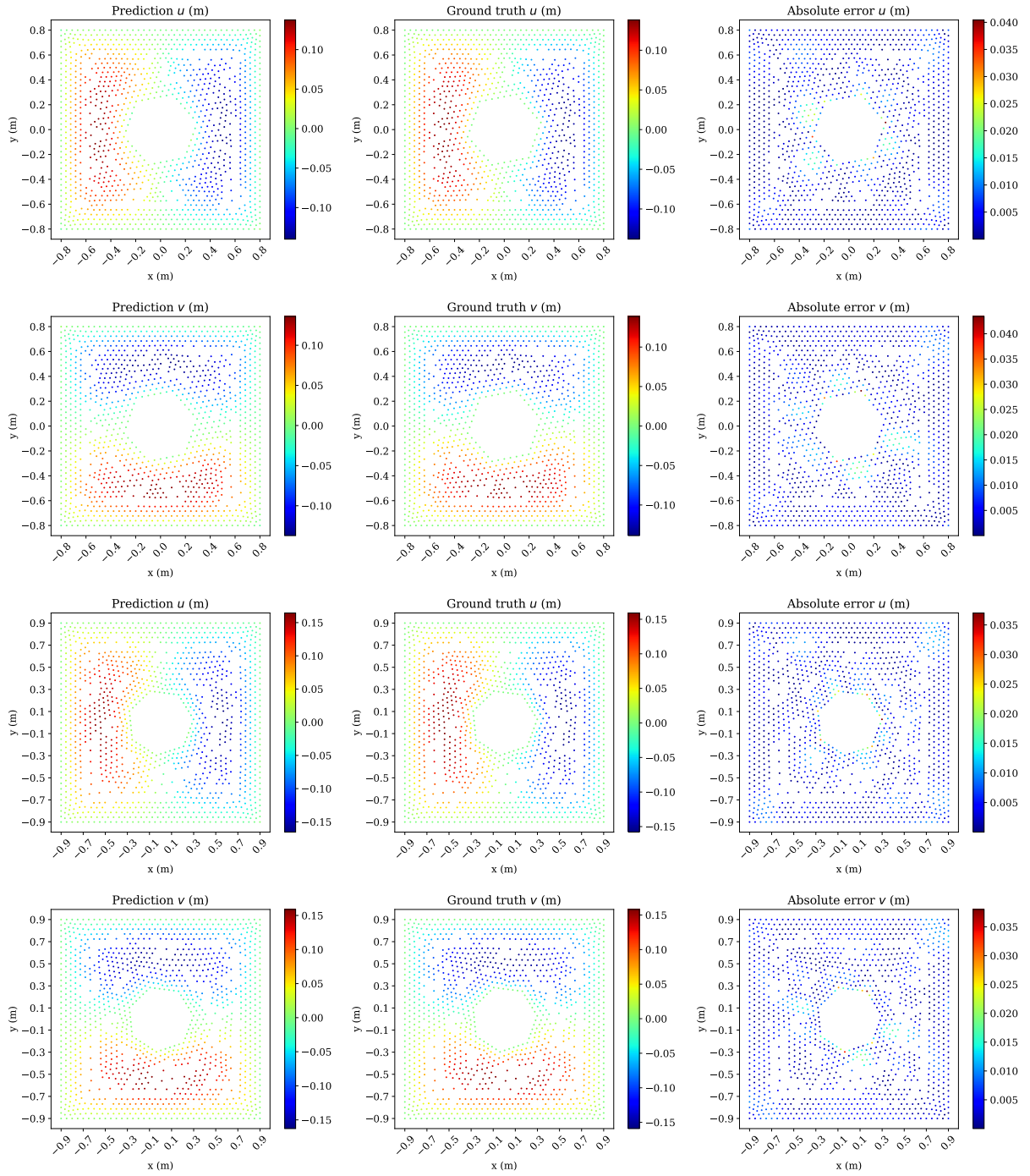


Figure 5: The second group of examples taken from the set $\Phi = \{V_i\}_{i=1}^{532}$, comparing the finite element solutions to the PIPN predictions for the displacement fields

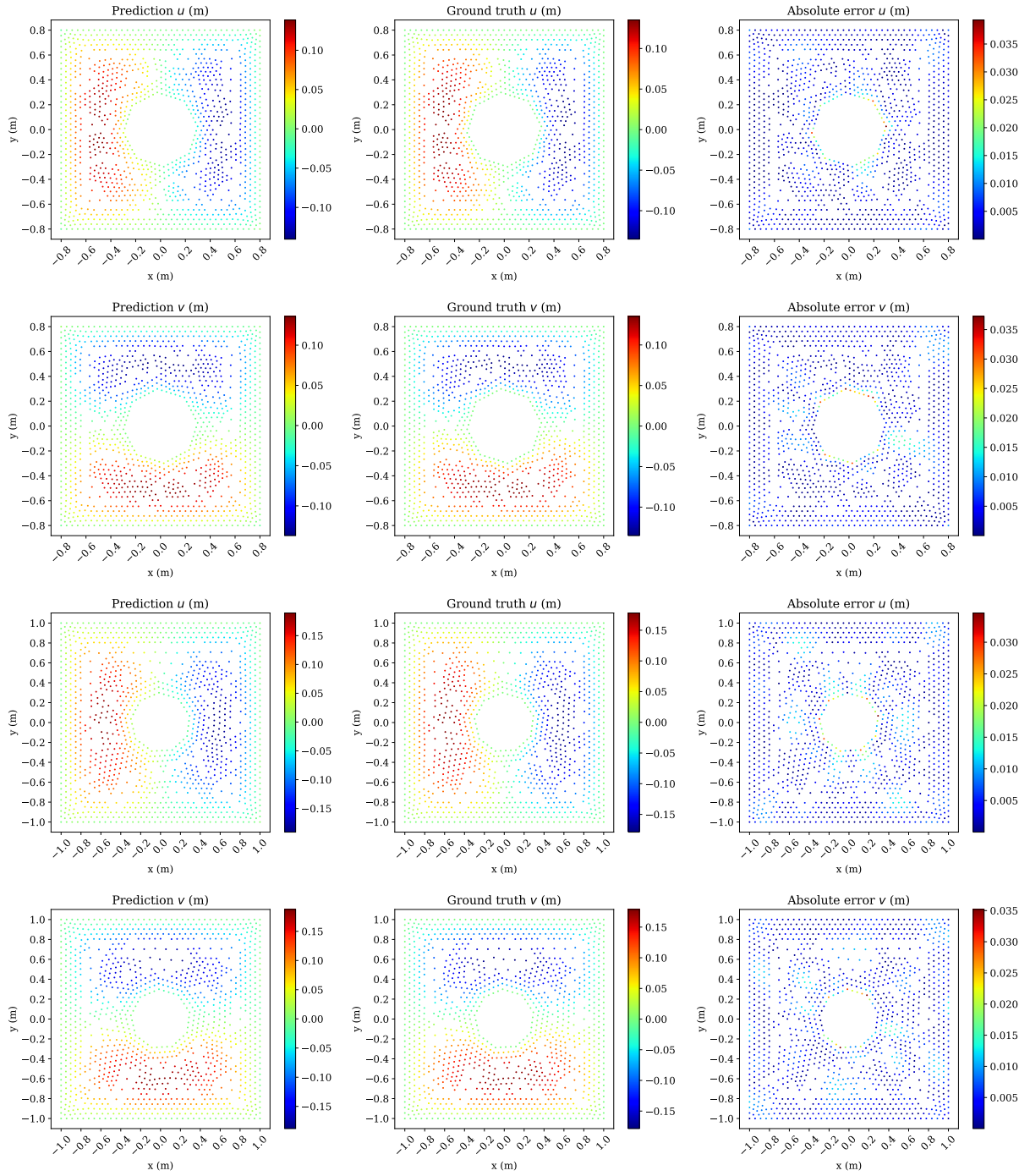


Figure 6: The third group of examples taken from the set $\Phi = \{V_i\}_{i=1}^{532}$, comparing the finite element solutions to the PIPN predictions for the displacement fields

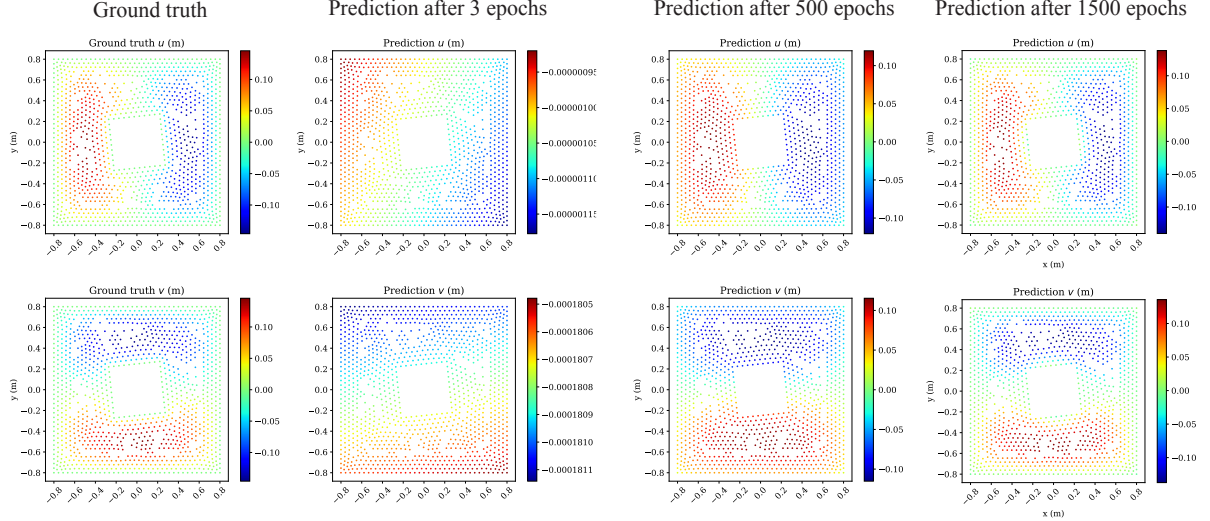


Figure 7: A comparison between the ground truth and prediction of PIPN for the displacement fields after 3, 500, and 1500 epochs

Table 3: Error analysis of the displacement fields for the domains of the set $\Phi = \{V_i\}_{i=1}^{532}$ for different batch sizes (B) and three different network sizes of $n_s = 1.0$, $n_s = 0.5$, and $n_s = 0.25$ when $\omega_{\text{sensor}} = 50 \text{ m}^{-1}$ and $\omega_{\text{momentum}} = 1 \text{ m}$. $\|\dots\|$ denotes the L^2 norm. The cross symbol (\times) indicates that the machine learning experiment is not doable due to a memory limitation.

Batch size (B)	$n_s = 1.0$	$n_s = 1.0$	$n_s = 0.5$	$n_s = 0.5$	$n_s = 0.25$	$n_s = 0.25$
	Average	Average	Average	Average	Average	Average
	$\ \tilde{u} - u\ /\ u\ $	$\ \tilde{v} - v\ /\ v\ $	$\ \tilde{u} - u\ /\ u\ $	$\ \tilde{v} - v\ /\ v\ $	$\ \tilde{u} - u\ /\ u\ $	$\ \tilde{v} - v\ /\ v\ $
7	8.56410E-2	8.58942E-2	8.40571E-2	8.90152E-2	1.00000	1.00000
14	8.24455E-2	7.84251E-2	8.71806E-2	7.68771E-2	9.99999E-1	1.00000
19	8.34842E-2	8.42466E-2	8.03585E-2	8.33552E-2	5.08574E-1	1.00000
28	8.11108E-2	8.60237E-2	7.44200E-2	7.40376E-2	3.24522E-1	3.45531E-1
38	8.69939E-2	9.05297E-2	8.45176E-2	8.20743E-2	3.68147E-1	3.69285E-1
76	\times	\times	3.77084E-1	3.78790E-1	1.00000	9.9997E-1
133	\times	\times	\times	\times	1.00000	5.05933E-1

3.2 Effect of batch size and network size

We first explore the effect of batch sizes (B) on the PIPN performance in this subsection. It is worthwhile to note that at each epoch, the geometries are shuffled and randomly divided into mini-batch, exactly similar to the scenario of fully supervised learning models. We collect the average relative pointwise errors (L^2 norm) of the displacement fields for the batch sizes (B) of 7, 14, 19, 28, 38, 76, and 133 for three different network sizes (n_s) of 1.0, 0.5, and 0.25 in Table 3. Note that due to the memory limitations, a few of these machine learning experiments are not doable such as the combination of a batch size of $B = 133$ with the network size of $n_s = 1.0$. According to Table 3, for a fixed network size of $n_s = 1.0$, the batch size (B) does not significantly affect the prediction accuracy. A similar story is true when the network size of $n_s = 0.5$ is taken, except for the batch size of $B = 76$, where the accuracy of the PIPN prediction notably decreases and the average relative pointwise errors (L^2 norm) of the displacement fields becomes approximately 37%. The optimal batch size (B) is 28 for this network size ($n_s = 0.5$). By reducing the network size to $n_s = 0.25$, the overall performance of PIPN sharply decreases. For batch sizes (B) of 7, 14, 19, 76, and 133, the PIPN prediction is completely off. For the batch sizes (B) of 28 and 38, although the average relative pointwise errors (L^2 norm) are less than 50%, the PIPN solution is not reliable. The lack of PIPN performance for the choice of $n_s = 0.25$ is further discussed at the end of this subsection. But it is concluded that it is important to first select a PIPN with a suitable size, before investigating the effect of the batch size (B). In other words, the effect of network size on PIPN is significantly more noticeable compared to the influence of the batch size.

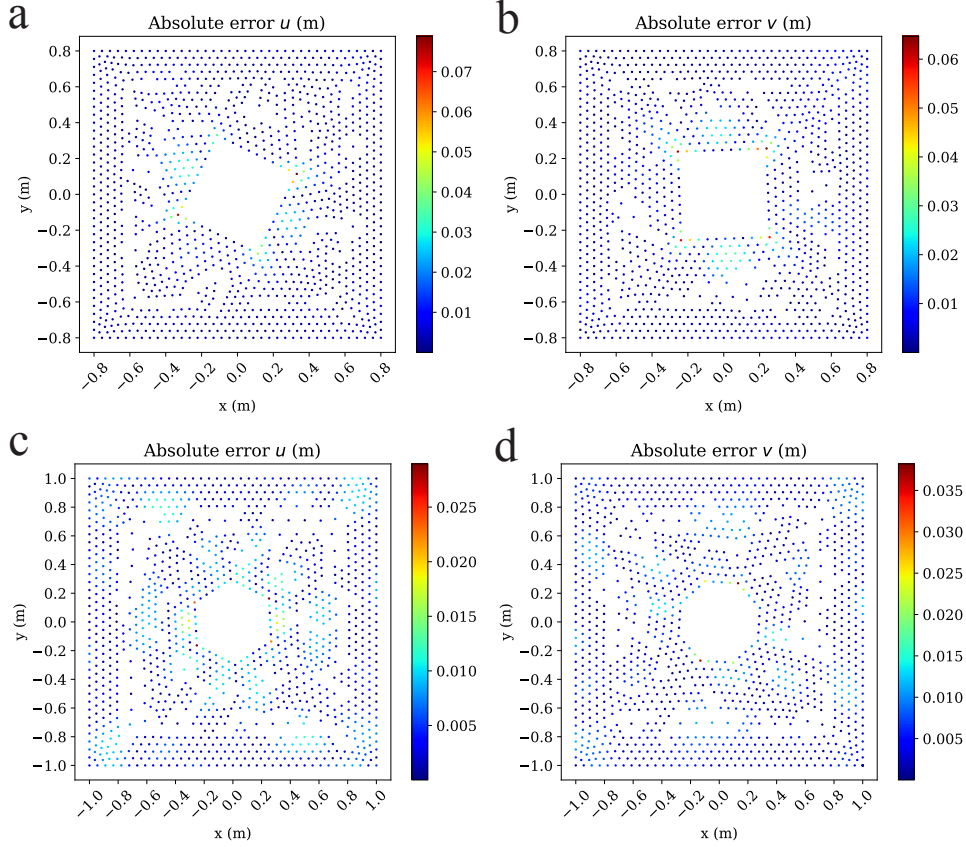


Figure 8: Distribution of absolute pointwise error when the relative pointwise error (L^2 norm) becomes (a) maximum for \tilde{u} , (b) maximum for \tilde{v} , (c) minimum for \tilde{u} , and (d) minimum for \tilde{v}

Table 4: Error analysis of the displacement fields for the domains of the set $\Phi = \{V_i\}_{i=1}^{532}$ for different network sizes (n_s) when $B = 19$, $\omega_{\text{sensor}} = 50 \text{ m}^{-1}$, and $\omega_{\text{momentum}} = 1 \text{ m}$. $\|\dots\|$ indicates the L^2 norm.

Network size (n_s)	Average $\frac{\ \tilde{u}-u\ }{\ u\ }$	Average $\frac{\ \tilde{v}-v\ }{\ v\ }$
0.125	1.00001	1.00000
0.25	5.08574E-1	1.00000
0.5	8.03585E-2	8.33552E-2
1.0	8.34842E-2	8.42466E-2
1.5	8.51296E-2	7.35883E-2
2.0	9.25092E-2	1.00152E-1
2.5	1.51389E-1	1.52311E-1

The evolution of the PIPN loss function (see Eq. 15) for the batch sizes (B) of 7, 14, 19, 28, 38, and 76 for the network size of $n_s = 0.5$ is shown in Fig. 9a. According to Fig. 9a, for the batch sizes (B) of 7, 14, 19, 28, and 38, although the loss function eventually converges to approximately the same value, the machine learning experiment with the batch size of $B = 19$ reaches this convergence with a significantly smaller number of epochs. Moreover, the PIPN loss associated with the batch size of $B = 76$ converges to a value larger than the other investigated batch sizes, as can be realized from Fig. 9a. This fact can be seen in another form by looking at the relative errors tabulated in Table 3 as already discussed.

Additionally, the effect of network size is carried out and outcomes are listed in Table 4. Based on the information listed in Table 4, for relatively small network sizes ($n_s = 0.125$, $n_s = 0.25$) and relatively large network sizes ($n_s = 2.0$, $n_s = 2.5$), the PIPN configuration experiences a higher level of errors compared to the moderate sizes of the network ($n_s = 0.5$, $n_s = 1.0$, $n_s = 1.5$). For a relatively small PIPN, the network is too simple and a bias (i.e., underfitting) takes place. For a relatively large PIPN, the number of data is not sufficient to well determine the weight matrix (\mathbf{W}) and bias vector (\mathbf{b}) of the network, and hence, the PIPN predictions suffer from the lack of accuracy.

Furthermore, the evolution of the total loss value over all the geometries of the set $\Phi = \{V_i\}_{i=1}^{532}$ is displayed for the network sizes (n_s) of 0.125, 0.25, 0.5, 1.0, 1.5, 2.0, and 2.5 in Fig. 9b. As can be seen in Fig. 9b, for

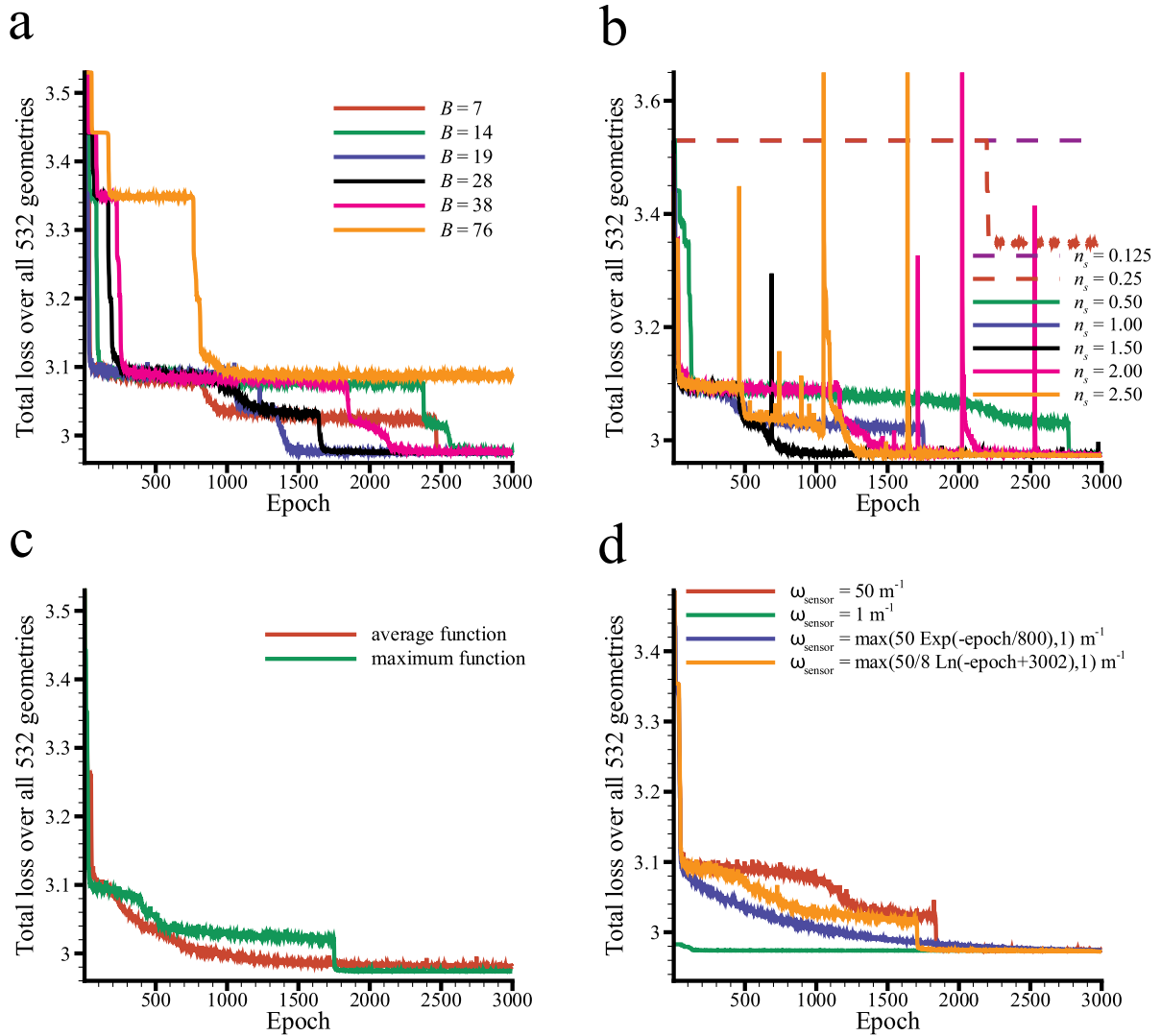


Figure 9: Evolution of the PIPN loss function **a** for different batch sizes (B); **b** for different network sizes (n_s); **c** for two different symmetric functions (see Eqs. 8–9); **d** for different setups of the weight of the sensor component in (ω_{sensor}) in the loss PIPN function (see Eqs. 16–19)

the network size (n_s) of 0.125, the training loss does not converge, leading to 100% relative errors as tabulated in Table 4. As discussed earlier, for the network sizes (n_s) of 0.5, 1.0, and 1.5, the relative errors of PIPN are approximately the same and smaller than other network size choices. Among these three selections, the network size (n_s) of 1.5 converges approximately after 800 epochs, while PIPN with the network size (n_s) of 0.5 converges after approximately 2800 epochs. For the network size (n_s) of 2.0 and 2.5, although the training loss converges, we observe a tremendous tendency for divergence and instability in the optimization process. The reason comes back to the fact that the number of data is not adequate for this choice of the PIPN size as explained in the previous paragraph.

3.3 Choice of a symmetric function in PIPN

We investigate the effectiveness of two different symmetric functions (see Eqs. 8–9) in the setting of the PIPN configuration. Specifically, we set the batch size of $B = 19$ and the network size of $n_s = 1.0$ with the weight of $\omega_{\text{sensor}} = 50 \text{ m}^{-1}$ for the sensor component in the PIPN loss function for this machine learning experiment. Figure 9c illustrates the evolution of the PIPN loss function (see Eq. 15) for the maximum and average as two symmetric functions for extracting global features of point clouds. For a fair comparison, the network size and the batch size are set the same in both experiments. As can be observed in Fig. 9c, the max function shows a better final performance compared to the average functions, though the loss with the average function initially drops faster than the loss function with the max function. However, a sharp decrease in the PIPN loss value with the maximum function occurs around approximately 1800 epochs such that this loss value becomes smaller than

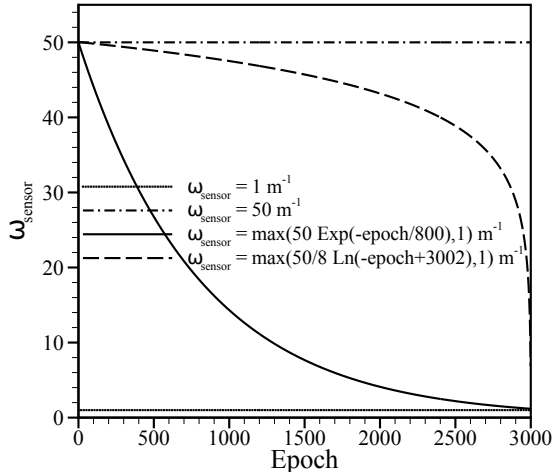


Figure 10: Evolution of the weight of the sensor component (ω_{sensor}) in the PIPN loss function during the training procedure for four different formulas (see Eqs. 16–19)

the corresponding value with the average function. Quantitatively, the average relative pointwise error (L^2 norm) of the displacement fields (u , v) in the x and y directions are respectively $4.69055\text{E}-1$ and $4.39773\text{E}-1$ for the average function while these errors are $8.34842\text{E}-2$ and $8.42466\text{E}-2$ for the maximum function.

We note that Qi, et al. [43, 44] used the maximum function for the purpose of object classification and segmentations in the area of computer graphics, and we observe here a higher performance with the maximum function in the area of computational mechanics as well. The reason can be explained as follows. As shown by Kashefi, et al. [29] for supervised learning, using the maximum function, boundary points of point clouds of the domains always contribute to the global feature in PointNet [43]. This is while the most variation from one geometry to another one happens also on boundaries. In this way, PIPN can more clearly distinguish the PDE solution depending on the geometric features of each domain of the set $\Phi = \{V_i\}_{i=1}^{532}$.

3.4 Effect of component weights in the PIPN loss function

We investigate four different formulas for the weight component of the sensor data in the PIPN loss function. More specifically, we set $\omega_0 = 50 \text{ m}^{-1}$ in Eq. 17, we set $\omega_1 = 50 \text{ m}^{-1}$ and $r_1 = 800$ in Eq. 18, and we set $\omega_2 = \frac{50}{8} \text{ m}^{-1}$ and $r_2 = 3002$ in Eq. 19. We display the evolution of the weight of the sensor component (ω_{sensor}) during training in Fig. 10 for these four different setups (Eqs. 16–19). The relative pointwise errors (L^2 norm) are tabulated in Table 5. In general, the best PIPN performance is when ω_{sensor} is larger than ω_{momentum} and decreases either logarithmically or not at all (see Eq. 17 and Fig. 9d as well as Eq. 18 and Fig. 9d).

Additionally, we plot the evolution of the PIPN loss function during training as a result of these four different formulas (see Eqs. 16–19). These results demonstrate that setting a reasonably higher weight for the sensor component of the loss function (i.e., ω_{sensor}) compared to the PDE component of the loss function (i.e., ω_{momentum}) even during the entire training procedure leads to more accurate outputs. Mathematically, because PIPN is not informed of any boundary conditions in this problem, there are infinite solutions to the governing PDEs and thus obtaining the right solution is challenging for PIPN. But by setting a higher weight for the sensor data, PIPN is forced to have a priority for satisfying the mismatch between the network output and sensor data; however, this enforcement makes it convenient to also satisfy the governing PDEs because PIPN looks for the PDE solutions in the space created by the sensor data (rather than a weakly unknown space).

Table 5: Error analysis of the displacement fields for the domains of the set $\Phi = \{V_i\}_{i=1}^{532}$ for different settings of weights ω_{sensor} in the loss PIPN function when $B = 28$ and $\omega_{\text{momentum}} = 1 \text{ m}$. $\|\dots\|$ shows the L^2 norm.

ω_{sensor}	Average $\frac{\ \tilde{u}-u\ }{\ u\ }$	Average $\frac{\ \tilde{v}-v\ }{\ v\ }$
1.0 m^{-1}	$3.72051\text{E}-1$	$3.75747\text{E}-1$
50.0 m^{-1}	$8.11108\text{E}-2$	$8.60237\text{E}-2$
$\max\left(50 \times \exp\left(\frac{-\text{epoch}}{800}\right), 1.0\right) \text{ m}^{-1}$	$3.71722\text{E}-1$	$3.71195\text{E}-1$
$\max\left(\frac{50}{8} \times \ln(-\text{epoch} + 3002), 1.0\right) \text{ m}^{-1}$	$9.81245\text{E}-2$	$9.63949\text{E}-2$

Additionally, we plot the evolution of the total PIPN loss over all geometries of the set $\Phi = \{V_i\}_{i=1}^{532}$ for four different setups of the sensor component weight (see Eqs. 16–19) in Fig. 9d. Comparing the deep learning experiment with the constant value of $\omega_{\text{sensor}} = 50 \text{ m}^{-1}$ (see Eq. 17) and the logarithmic function (see Eq. 19), a convergence with fewer epochs happens for the logarithmic function, as can be seen in Fig. 9d. Note that according to Table 5, PIPN demonstrates a higher performance for the two mentioned choices of ω_{sensor} in comparison with the constant value of $\omega_{\text{sensor}} = 1 \text{ m}^{-1}$ (see Eq. 16) and the exponential function (see Eq. 18). Moreover, the PIPN loss evolution with the exponential function for presenting ω_{sensor} (see Eq. 18) has a smooth decay and converges to a value, which is slightly higher than the convergence values of deep learning experiments with the constant value of $\omega_{\text{sensor}} = 50 \text{ m}^{-1}$ (see Eq. 17) and the logarithmic function (see Eq. 19). For the choice of the constant value of $\omega_{\text{sensor}} = 1 \text{ m}^{-1}$ (see Eq. 16), the initial loss is smaller than the other three options simply because the weight of the sensor component in the loss function (see Eq. 15) is scaled down by a factor of 50. However, the initial loss decreases with a very gentle slope up to 3000 epochs and thus there is a 38% average relative error as reported in Table 5.

4 Summary and conclusions

Generally speaking, there are two different deep learning categories in the area of computational mechanics: weakly supervised learning models, requiring sparse labeled data (see e.g., [47]) and fully supervised learning models, requiring plentiful labeled data [55]. A specific class of supervised learning models is physics-informed neural networks (PINNs) [47]. From an industrial point of view, an ideal deep learning framework should contain the ability to predict desired fields over hundreds, or even thousands, of domains with various geometries for the goal of swiftly optimizing geometric designs. Regular PINNs are applicable to the prediction of desired fields on a single geometry, whereas fully supervised learning models are used to predict desired fields on a few hundred geometries. In this sense, there is a gap between the weakly supervised learning and supervised learning models. Physics-informed PointNet (PIPNet) [26] is a novel class of physics-informed deep learning algorithms that fills this gap. PIPNet requires sparse label data but potentially is able to predict desired fields on a few hundred geometries.

In 2022, Kashefi and Mukerji [26] proposed PIPNet and employed it to solve incompressible flow and thermal fields over 108 domains with different geometries, simultaneously. Furthermore, they only investigated the batch sizes of 1, 2, 3, and 4 for the natural convection problem and the batch size of 13 for the method of manufactured solutions [26]. In the current article, we tried for the first time to explore the underlying capacity of PIPNet in terms of the number of geometries that desired fields can be predicted on, simultaneously, and also to investigate if PIPNet (as a weakly supervised learning model) is able to compete with fully supervised learning models from this point of view or not. We answered this question by considering a linear elasticity problem and more specifically plane stress conditions.

Given our computational resources, we showed that PIPNet was able to successfully predict the displacement fields over 532 domains with different geometries, simultaneously. The average relative pointwise error (L^2 norm) was approximately 9% over the set. For the first time, we comprehensively explored the effects of batch size on the PIPNet performance. By the term “batch size”, we meant the number of geometries that were fed into PIPNet at each sub-epoch. Particularly, we executed batch sizes of 7, 14, 19, 28, 38, 76, and 133. In addition, we pioneered introducing a global parameter for controlling the network size of PIPNet. Moreover, we systematically investigated for the first time the effect of this parameter on the accuracy of the PIPNet predictions. It was concluded that the network size plays a more important role in controlling the PIPNet performance compared to the batch size. It was observed that the network size should be compatible with the size of data (i.e., the number of geometries). In fact, we realized that when a suitable size for PIPNet was selected, the effect of batch size on the output predictions by PIPNet was insignificant. However, the batch size affected the convergence rate. Furthermore, we studied for the first time the accuracy of the displacement fields predicted by the PIPNet methodology as a result of different constant weights and dynamics weights (i.e., as a function of epoch) for the component of the partial differential equations and the component of the sparse labeled data in the PIPNet loss function. It was concluded that setting a constant higher weight for the component of the sparse labeled data compared to the component of the partial differential equations leads to higher prediction accuracy.

Declaration of competing interest

The authors declare that they have no known competing financial interests or personal relationships that could have appeared to influence the work reported in this paper.

Data availability

The data and the developed Python code are available on the following GitHub repository: <https://github.com/Ali-Stanford/PhysicsInformedPointNetElasticity>. One may also generate the code using ChatGPT [27] by providing a description of the PIPNet architecture detailed in this article.

Acknowledgements

The authors acknowledge funding by the Shell-Stanford Collaborative Project on Digital Rock Physics 2.0 for supporting this research project. Additionally, we would like to thank the Stanford Research Computing Center for supporting our studies by providing computing resources. We wish to also thank the reviewers for their insightful comments and suggestions.

References

- [1] Martín Abadi, Ashish Agarwal, Paul Barham, Eugene Brevdo, Zhifeng Chen, Craig Citro, Greg S. Corrado, Andy Davis, Jeffrey Dean, Matthieu Devin, Sanjay Ghemawat, Ian Goodfellow, Andrew Harp, Geoffrey Irving, Michael Isard, Yangqing Jia, Rafal Jozefowicz, Lukasz Kaiser, Manjunath Kudlur, Josh Levenberg, Dan Mané, Rajat Monga, Sherry Moore, Derek Murray, Chris Olah, Mike Schuster, Jonathon Shlens, Benoit Steiner, Ilya Sutskever, Kunal Talwar, Paul Tucker, Vincent Vanhoucke, Vijay Vasudevan, Fernanda Viégas, Oriol Vinyals, Pete Warden, Martin Wattenberg, Martin Wicke, Yuan Yu, and Xiaoqiang Zheng. TensorFlow: Large-scale machine learning on heterogeneous systems, 2015. Software available from tensorflow.org.
- [2] Muhammad M Almajid and Moataz O Abu-Al-Saud. Prediction of porous media fluid flow using physics informed neural networks. *Journal of Petroleum Science and Engineering*, 208:109205, 2022.
- [3] Jinshuai Bai, Timon Rabczuk, Ashish Gupta, Laith Alzubaidi, and Yuantong Gu. A physics-informed neural network technique based on a modified loss function for computational 2d and 3d solid mechanics. *Computational Mechanics*, pages 1–20, 2022.
- [4] Yoshua Bengio. Practical recommendations for gradient-based training of deep architectures. In *Neural networks: Tricks of the trade*, pages 437–478. Springer, 2012.
- [5] Hamed Bolandi, Gautam Sreekumar, Xuyang Li, Nizar Lajnef, and Vishnu Naresh Boddeti. Physics informed neural network for dynamic stress prediction. *arXiv preprint arXiv:2211.16190*, 2022.
- [6] Aaron B Buhendwa, Stefan Adami, and Nikolaus A Adams. Inferring incompressible two-phase flow fields from the interface motion using physics-informed neural networks. *Machine Learning with Applications*, 4:100029, 2021.
- [7] Shengze Cai, Zhicheng Wang, Sifan Wang, Paris Perdikaris, and George Em Karniadakis. Physics-informed neural networks for heat transfer problems. *Journal of Heat Transfer*, 143(6):060801, 2021.
- [8] Zeyu Cao, Wen Yao, Wei Peng, Xiaoya Zhang, and Kairui Bao. Physics-informed mta-unet: Prediction of thermal stress and thermal deformation of satellites. *Aerospace*, 9(10):603, 2022.
- [9] Wei Chen, Kevin Chiu, and Mark Fuge. Aerodynamic design optimization and shape exploration using generative adversarial networks. In *AIAA Scitech 2019 Forum*, page 2351, 2019.
- [10] Ryan S DeFever, Colin Targonski, Steven W Hall, Melissa C Smith, and Sapna Sarupria. A generalized deep learning approach for local structure identification in molecular simulations. *Chemical science*, 10(32):7503–7515, 2019.
- [11] Hamidreza Eivazi, Mojtaba Tahani, Philipp Schlatter, and Ricardo Vinuesa. Physics-informed neural networks for solving reynolds-averaged navier–stokes equations. *Physics of Fluids*, 34(7):075117, 2022.
- [12] Juan Fernández, Juan Chiachío, Manuel Chiachío, José Barros, and Matteo Corbetta. Physics-guided bayesian neural networks by abc-ss: Application to reinforced concrete columns. *Engineering Applications of Artificial Intelligence*, 119:105790, 2023.
- [13] Moritz Flaschel, Siddhant Kumar, and Laura De Lorenzis. Discovering plasticity models without stress data. *npj Computational Materials*, 8(1):91, 2022.
- [14] Han Gao, Luning Sun, and Jian-Xun Wang. PhyGeoNet: physics-informed geometry-adaptive convolutional neural networks for solving parameterized steady-state PDEs on irregular domain. *Journal of Computational Physics*, 428:110079, 2021.
- [15] Ian Goodfellow, Yoshua Bengio, and Aaron Courville. *Deep learning*. MIT press, 2016.
- [16] Ehsan Haghghat, Maziar Raissi, Adrian Moure, Hector Gomez, and Ruben Juanes. A physics-informed deep learning framework for inversion and surrogate modeling in solid mechanics. *Computer Methods in Applied Mechanics and Engineering*, 379:113741, 2021.
- [17] GaoYuan He, YongXiang Zhao, and ChuLiang Yan. Mflp-pinn: A physics-informed neural network for multiaxial fatigue life prediction. *European Journal of Mechanics-A/Solids*, 98:104889, 2023.
- [18] Ameya D Jagtap, Ehsan Kharazmi, and George Em Karniadakis. Conservative physics-informed neural networks on discrete domains for conservation laws: Applications to forward and inverse problems. *Computer Methods in Applied Mechanics and Engineering*, 365:113028, 2020.
- [19] Ameya D Jagtap, Zhiping Mao, Nikolaus Adams, and George Em Karniadakis. Physics-informed neural networks for inverse problems in supersonic flows. *Journal of Computational Physics*, 466:111402, 2022.

- [20] Hyogu Jeong, Jinshuai Bai, CP Batuwatta-Gamage, Charith Rathnayaka, Ying Zhou, and YuanTong Gu. A physics-informed neural network-based topology optimization (pinnto) framework for structural optimization. *Engineering Structures*, 278:115484, 2023.
- [21] Weiqi Ji, Weilun Qiu, Zhiyu Shi, Shaowu Pan, and Sili Deng. Stiff-pinn: Physics-informed neural network for stiff chemical kinetics. *The Journal of Physical Chemistry A*, 125(36):8098–8106, 2021.
- [22] Jindong Jiang, Jiawei Zhao, Shanmin Pang, Fodil Meraghni, Ali Siadat, and Qiang Chen. Physics-informed deep neural network enabled discovery of size-dependent deformation mechanisms in nanostructures. *International Journal of Solids and Structures*, 236:111320, 2022.
- [23] Xiaowei Jin, Shengze Cai, Hui Li, and George Em Karniadakis. NSFnets (Navier-Stokes flow nets): Physics-informed neural networks for the incompressible Navier-Stokes equations. *Journal of Computational Physics*, 426:109951, 2021.
- [24] Ibrahim Kandel and Mauro Castelli. The effect of batch size on the generalizability of the convolutional neural networks on a histopathology dataset. *ICT express*, 6(4):312–315, 2020.
- [25] Ali Kashefi and Tapan Mukerji. Point-cloud deep learning of porous media for permeability prediction. *Physics of Fluids*, 33(9):097109, 2021.
- [26] Ali Kashefi and Tapan Mukerji. Physics-informed PointNet: A deep learning solver for steady-state incompressible flows and thermal fields on multiple sets of irregular geometries. *Journal of Computational Physics*, 468:111510, 2022.
- [27] Ali Kashefi and Tapan Mukerji. Chatgpt for programming numerical methods. *Journal of Machine Learning for Modeling and Computing*, 4(2), 2023.
- [28] Ali Kashefi and Tapan Mukerji. Prediction of fluid flow in porous media by sparse observations and physics-informed pointnet. *Neural Networks*, 167:80–91, 2023.
- [29] Ali Kashefi, Davis Rempe, and Leonidas J Guibas. A point-cloud deep learning framework for prediction of fluid flow fields on irregular geometries. *Physics of Fluids*, 33(2):027104, 2021.
- [30] Nitish Shirish Keskar, Dheevatsa Mudigere, Jorge Nocedal, Mikhail Smelyanskiy, and Ping Tak Peter Tang. On large-batch training for deep learning: Generalization gap and sharp minima. *arXiv preprint arXiv:1609.04836*, 2016.
- [31] Diederik P Kingma and Jimmy Ba. Adam: A method for stochastic optimization. *arXiv preprint arXiv:1412.6980*, 2014.
- [32] Min Lin, Qiang Chen, and Shuicheng Yan. Network in network. *arXiv preprint arXiv:1312.4400*, 2013.
- [33] Kevin Linka, Amelie Schäfer, Xuhui Meng, Zongren Zou, George Em Karniadakis, and Ellen Kuhl. Bayesian physics informed neural networks for real-world nonlinear dynamical systems. *Computer Methods in Applied Mechanics and Engineering*, 402:115346, 2022.
- [34] Kingyu Liu, Charles R Qi, and Leonidas J Guibas. FlowNet3D: Learning Scene Flow in 3D Point Clouds. *Proc. Computer Vision and Pattern Recognition (CVPR)*, IEEE, 2019.
- [35] Qin Lou, Xuhui Meng, and George Em Karniadakis. Physics-informed neural networks for solving forward and inverse flow problems via the Boltzmann-BGK formulation. *Journal of Computational Physics*, 447:110676, 2021.
- [36] Zhiping Mao, Ameya D Jagtap, and George Em Karniadakis. Physics-informed neural networks for high-speed flows. *Computer Methods in Applied Mechanics and Engineering*, 360:112789, 2020.
- [37] Dominic Masters and Carlo Luschi. Revisiting small batch training for deep neural networks. *arXiv preprint arXiv:1804.07612*, 2018.
- [38] Sijun Niu, Enrui Zhang, Yuri Bazilevs, and Vikas Srivastava. Modeling finite-strain plasticity using physics-informed neural network and assessment of the network performance. *Journal of the Mechanics and Physics of Solids*, 172:105177, 2023.
- [39] Hanqing Ouyang, Zhicheng Zhu, Kuangqi Chen, Beichen Tian, Biao Huang, and Jia Hao. Reconstruction of hydrofoil cavitation flow based on the chain-style physics-informed neural network. *Engineering Applications of Artificial Intelligence*, 119:105724, 2023.
- [40] Ravi G Patel, Indu Manickam, Nathaniel A Trask, Mitchell A Wood, Myoungkyu Lee, Ignacio Tomas, and Eric C Cyr. Thermodynamically consistent physics-informed neural networks for hyperbolic systems. *Journal of Computational Physics*, 449:110754, 2022.
- [41] Charles R Qi, Or Litany, Kaiming He, and Leonidas J Guibas. Deep hough voting for 3d object detection in point clouds. *arXiv preprint arXiv:1904.09664*, 2019.
- [42] Charles R Qi, Wei Liu, Chenxia Wu, Hao Su, and Leonidas J Guibas. Frustum pointnets for 3d object detection from rgb-d data. In *Proceedings of the IEEE conference on computer vision and pattern recognition*, pages 918–927, 2018.

- [43] Charles R Qi, Hao Su, Kaichun Mo, and Leonidas J Guibas. Pointnet: Deep learning on point sets for 3d classification and segmentation. In *Proceedings of the IEEE conference on computer vision and pattern recognition*, pages 652–660, 2017.
- [44] Charles Ruizhongtai Qi, Li Yi, Hao Su, and Leonidas J Guibas. PointNet++: Deep hierarchical feature learning on point sets in a metric space. In *Advances in neural information processing systems*, pages 5099–5108, 2017.
- [45] Rundi Qiu, Renfang Huang, Yao Xiao, Jingzhu Wang, Zhen Zhang, Jieshun Yue, Zhong Zeng, and Yiwei Wang. Physics-informed neural networks for phase-field method in two-phase flow. *Physics of Fluids*, 34(5):052109, 2022.
- [46] Yitao Qiu, Prajwal Kammardi Arunachala, and Christian Linder. Sensenet: A physics-informed deep learning model for shape sensing. *Journal of Engineering Mechanics*, 149(3):04023002, 2023.
- [47] Maziar Raissi, Paris Perdikaris, and George E Karniadakis. Physics-informed neural networks: A deep learning framework for solving forward and inverse problems involving nonlinear partial differential equations. *Journal of Computational Physics*, 378:686–707, 2019.
- [48] Chengping Rao, Hao Sun, and Yang Liu. Physics-Informed Deep Learning for Computational Elastodynamics without Labeled Data. *Journal of Engineering Mechanics*, 147(8):04021043, 2021.
- [49] Pu Ren, Chengping Rao, Yang Liu, Jian-Xun Wang, and Hao Sun. PhyCRNet: Physics-informed convolutional-recurrent network for solving spatiotemporal PDEs. *Computer Methods in Applied Mechanics and Engineering*, 389:114399, 2022.
- [50] Shahed Rezaei, Ali Harandi, Ahmad Moeineddin, Bai-Xiang Xu, and Stefanie Reese. A mixed formulation for physics-informed neural networks as a potential solver for engineering problems in heterogeneous domains: comparison with finite element method. *Computer Methods in Applied Mechanics and Engineering*, 401:115616, 2022.
- [51] Vinothkumar Sekar, Qinghua Jiang, Chang Shu, and Boo Cheong Khoo. Fast flow field prediction over airfoils using deep learning approach. *Physics of Fluids*, 31(5):057103, 2019.
- [52] Zhengyuan Shen, Yangzesheng Sun, Timothy P Lodge, and J Ilja Siepmann. Development of a pointnet for detecting morphologies of self-assembled block oligomers in atomistic simulations. *The Journal of Physical Chemistry B*, 125(20):5275–5284, 2021.
- [53] Saurabh Balkrishna Tandale, Franz Bamer, Bernd Markert, and Marcus Stoffel. Physics-based self-learning recurrent neural network enhanced time integration scheme for computing viscoplastic structural finite element response. *Computer Methods in Applied Mechanics and Engineering*, 401:115668, 2022.
- [54] Hugues Thomas, Charles R Qi, Jean-Emmanuel Deschaud, Beatriz Marcotegui, François Goulette, and Leonidas J Guibas. Kpconv: Flexible and deformable convolution for point clouds. In *Proceedings of the IEEE/CVF International Conference on Computer Vision*, pages 6411–6420, 2019.
- [55] Nils Thuerey, Konstantin Weïßenow, Lukas Prantl, and Xiangyu Hu. Deep Learning Methods for Reynolds-Averaged Navier–Stokes Simulations of Airfoil Flows. *AIAA Journal*, pages 1–12, 2019.
- [56] Shashank Reddy Vadyala, Sai Nethra Betgeri, John C Matthews, and Elizabeth Matthews. A review of physics-based machine learning in civil engineering. *Results in Engineering*, page 100316, 2021.
- [57] Tongsheng Wang, Zhu Huang, Zhongguo Sun, and Guang Xi. Reconstruction of natural convection within an enclosure using deep neural network. *International Journal of Heat and Mass Transfer*, 164:120626, 2021.
- [58] Yue Wang, Yongbin Sun, Ziwei Liu, Sanjay E Sarma, Michael M Bronstein, and Justin M Solomon. Dynamic graph cnn for learning on point clouds. *Acm Transactions On Graphics (tog)*, 38(5):1–12, 2019.
- [59] Yuting Weng and Dezhi Zhou. Multiscale physics-informed neural networks for stiff chemical kinetics. *The Journal of Physical Chemistry A*, 126(45):8534–8543, 2022.
- [60] Wensi Wu, Mitchell Daneker, Matthew A Jolley, Kevin T Turner, and Lu Lu. Effective data sampling strategies and boundary condition constraints of physics-informed neural networks for identifying material properties in solid mechanics. *arXiv preprint arXiv:2211.15423*, 2022.
- [61] Zixue Xiang, Wei Peng, Xiaohu Zheng, Xiaoyu Zhao, and Wen Yao. Self-adaptive loss balanced physics-informed neural networks for the incompressible navier-stokes equations. *arXiv preprint arXiv:2104.06217*, 2021.
- [62] Chen Xu, Ba Trung Cao, Yong Yuan, and Günther Meschke. Transfer learning based physics-informed neural networks for solving inverse problems in engineering structures under different loading scenarios. *Computer Methods in Applied Mechanics and Engineering*, 405:115852, 2023.
- [63] Hui Xu, Wei Zhang, and Yong Wang. Explore missing flow dynamics by physics-informed deep learning: The parameterized governing systems. *Physics of Fluids*, 33(9):095116, 2021.
- [64] Liu Yang, Xuhui Meng, and George Em Karniadakis. B-pinns: Bayesian physics-informed neural networks for forward and inverse pde problems with noisy data. *Journal of Computational Physics*, 425:109913, 2021.

- [65] Jeremy Yu, Lu Lu, Xuhui Meng, and George Em Karniadakis. Gradient-enhanced physics-informed neural networks for forward and inverse pde problems. *Computer Methods in Applied Mechanics and Engineering*, 393:114823, 2022.
- [66] Lei Yuan, Yi-Qing Ni, Xiang-Yun Deng, and Shuo Hao. A-pinn: Auxiliary physics informed neural networks for forward and inverse problems of nonlinear integro-differential equations. *Journal of Computational Physics*, 462:111260, 2022.